Secondary Flows In A Faraday MHD Channel

Author(s): R. C. Goforth and C. H. Kruger

Session Name: Generators C

SEAM: 28 (1990)

SEAM EDX URL: https://edx.netl.doe.gov/dataset/seam-28

EDX Paper ID: 1439

SECONDARY FLOWS IN MHD CHANNELS

R. C. Goforth   C. H. Kruger
High Temperature Gasdynamics Laboratory
Stanford University
Stanford, CA 94305-3032

ABSTRACT

Secondary flows in MHD channels may significantly affect the plasma momentum, thermal, and electrical behavior. Several series of experiments have been conducted in the Stanford 2 MW-thermal MHD channel to investigate the nature of these secondary flows and their effects. Initial experiments were conducted in a "Hall configuration", with a pair of electrodes at the upstream end of the channel connected through an external load to a pair of electrodes at the downstream end. A controlled current was driven through the plasma using external power supplies. This configuration allowed a relatively straightforward interpretation of the measured secondary flowfield.

The most recent series of experiments were run in a segmented Faraday configuration. For this configuration, the Hall effect creates the axial currents that drive the secondary flows. In the absence of current leakage through the sidewalls, the net Hall current is zero but the local Hall current is generally non-zero and may be large. The channel had 13 electrode pairs and a 5×10 cm^2 cross-section. External power supplies were used to augment the transverse currents so that current densities of the order 1 A/cm^2 could be achieved.

Laser-Doppler anemometry (LDA) was used to directly measure the secondary flows near the downstream end of the channel. The effect of the secondary flows on boundary-layer voltage drops and on electrode temperatures was also measured.

1. INTRODUCTION

In open-cycle MHD power generator channels, the flow of the combustion plasma through a transverse magnetic field experiences nonuniform Lorentz forces in the direction mutually perpendicular to the channel axis and the magnetic field. These forces may cause secondary flows to develop as the flow progresses down the region of electromagnetic interaction. For conditions which would be typical of a commercial-scale MHD generator, the secondary flows have been predicted to be of substantial magnitude with transverse velocities greater than 10% of the bulk velocity, depending on conditions[1,2,3]. The predicted consequences of secondary flows include the development of significant asymmetries in the profiles of axial velocity and of temperature, with resultant effects on wall heat transfer and electrode voltage drops.

Girshick and Kruger[4] made the first direct, quantitative measurements of secondary flow in a combustion MHD channel. These measurements were made in the same laboratory-scale channel used in the present work. An applied Hall current and a relatively low axial velocity resulted in a level of electromagnetic interaction comparable to anticipated levels in the core of a commercial-scale MHD generator.

Laser-Doppler anemometry measurements showed peak transverse velocities of greater than 20% of the bulk velocity. This secondary flow strongly skewed the axial velocity and turbulence intensity distributions and significantly affected electrode voltage drops and surface temperatures. The region near the electrode toward which secondary flow convected hot core fluid was almost twice as conductive as the region adjacent to the opposite electrode. Similarly, the secondary flow increased the heat flux to one electrode wall while decreasing it to the opposite wall.

The measurements by Girshick and Kruger directly confirmed the presence of significant secondary flow, its effects, and the possibility of simulating electromagnetic interaction levels comparable to those in full-scale generators, with a laboratory device. Further work at Stanford has studied the sensitivity of the level of the secondary flow to interaction level and wall temperature[5] and investigated the structure of the secondary flowfield for the Hall-type configuration[6]. The most recent series of experiments were run in a segmented Faraday configuration. In these experiments, velocities, electrode voltage drops, and electrode temperature changes were measured for a range of interaction levels.

In this paper we review some of the results from the previous Hall-type configuration experiments and use a simple two-dimensional model to help explain some of the features of the observed flowfield. Additionally, we report the results of the segmented Faraday channel experiments.

2. THEORETICAL BACKGROUND

The strength and structure of secondary flows in MHD generators are determined by many effects. This section describes first order models of secondary flow development for the two electrical configurations for which secondary flows have been directly measured in the Stanford M-2 channel.

The most important vorticity generation mechanism is the nonuniformity in the direction of the applied magnetic field of the axial current density J_x. The fluid vorticity equation in the axial direction, neglecting density gradient effects, and for the case of uniform applied magnetic field in the z-direction, is given by

$$\rho\frac{D\Omega_x}{Dt}=B\frac{\partial J_x}{\partial z}+(viscous\ terms)\quad ,$$

where ρ is the fluid density, B is the applied magnetic flux density, and Ω_x is the axial vorticity defined by

$$\Omega_x=\frac{\partial w}{\partial y}-\frac{\partial v}{\partial z}\quad ,$$

where v and w are the y and z-directed velocities, respectively.

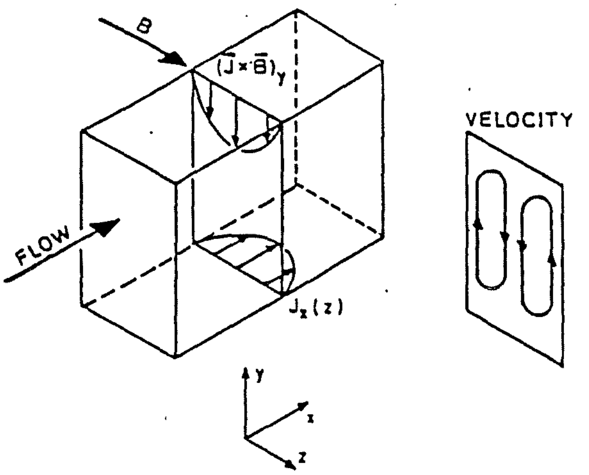

Figure 1 *Secondary Flow Mechanism for Hall Generators.*

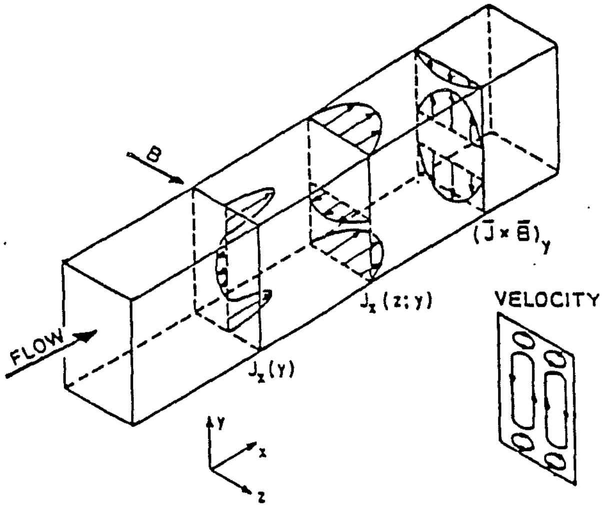

Figure 2 *Secondary Flow Mechanism for Segmented Faraday Generator.*

For Hall generators, the axial current is everywhere positive. Figure 1 shows the qualitative secondary flow generation mechanism for this configuration. For a combustion MHD channel, the plasma core has a higher temperature and conductivity than the plasma near the sidewalls thus creating a nonuniformity in the axial current. As shown in the figure, a $J_x \times B$ Lorentz force acts in the negative-y direction. For the first order profile of J_x shown, the nonuniform transverse Lorentz force creates a two cell rotation of the fluid in the cross plane.

For a generator connected in a segmented Faraday configuration, the net flow of Hall current is zero provided there is no axial leakage. The local Hall current will, however, generally be non-zero due to the Hall effect and may be large[7]. Figure 2 shows a first order axial current distribution for a segmented Faraday generator and shows the resultant secondary flowfield. For this simple case, a six-cell secondary flowfield is generated.

The first order secondary flow mechanisms depicted in Figures 1 and 2 neglect the coupling of the axial current distribution with the secondary flow. In the Hall geometry, for example, the secondary flow will distort a current distribution that starts out as in Figure 1, by sweeping hot core fluid to the sides in the bottom region of the channel and cooler fluid from near the sidewall into the z-center in the top region. Since the conductivity and hence the current density are strong functions of temperature, the current density profile flattens in the bottom and develops an "M"-shape profile in the top[6]. These distortions both tend to reduce the driving force for the vorticity except near the sidewalls.

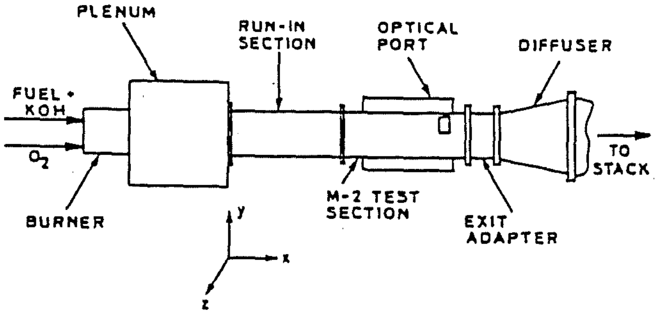

Figure 3 *M-2 Flow train.*

3. EXPERIMENTAL APPARATUS AND PROCEDURE

3.1 Flow Train Description and Run Conditions

Figure 3 shows a schematic of the High Temperature Gasdynamics Laboratory M-2 flow train. The M-2 facility as configured for the experiments to date consists of a combustor with a nominal 2-MW thermal input rating, a mixing plenum, a nozzle, a rectangular duct, a diffuser, and an exhaust system including a scrubber and a stack. The rectangular duct consists of a run-in section and the active channel itself, which is enclosed in a 2.6 Tesla water-cooled, copper-coil magnet. Table I gives the channel dimensions and nominal run conditions. The plasma results from the combustion of ethyl alcohol (C_2H_5OH) burned in pure oxygen at a stoichiometry of 1.05 (fuel rich). The fuel is seeded with potassium hydroxide (KOH), such that potassium constitutes 2.1% of the total

Table I Channel Geometry and Run Conditions

Channel geometry

Component	Dimensions (cm)
Combustor	D = 8.9, L = 36.8
Plenum	H = 22.9, W = 17.8, L = 48.3
Nozzle	H = 5.08 (10.16)*, W = 5.08, L = 2.5
Run-in section	H = 5.08 (10.16)*, W = 5.08, L = 50.8
Active channel	H = 5.08 (10.16)*, W = 5.08, L = 74.9
Extender section	H = 5.08 (10.16)*, W = 5.08, L = 20.3
Diffuser	H = 13.3, W = 6.4 expanding to 13.3, L = 43.2
Transfer tube	D = 25.4, L = 290

Distances from nozzle exit (cm)	
Active channel entrance	50.8
Center of first electrode	64.1
Velocity measurement plane	108.9
Center of last electrode	109.9

Electrodes: W = 5.08 cm, L = 1.91 cm.

D, diameter; H, height; W, width; L, length

Run conditions

Fuel	Ethyl Alcohol
N_2/O_2 ratio	0
Stoichiometry	1.05 (fuel rich)
Seed	Potassium hydroxide
Potassium mass fraction in reactants	2.1%
Total flow rate	55 (110)* g/s
Reynolds number (based on hydraulic diameter)	1.3 (1.95)* × 10^4
Calculated core conditions at nozzle exit	
Velocity	174 m/s
Temperature	2750 K
Mass density	0.122 kg/s
Mach number	.17
Electrical conductivity	14 S/m
Electron mobility	.37 $m^2/V{\cdot}s$
Channel conditions	
Wall temperatures	
Insulator	1900 K
Electrodes	1000 K
Magnetic induction	2.5 T
Electron Hall parameter	0.8

* Segmented Faraday Configuration Experiments

products by mass. The calculated nozzle exit velocity is approximately 170 m/s and the total flow rate at a calculated nozzle exit temperature of 2750 K corresponds to a Reynolds number (based on hydraulic diameter) of approximately $1.5{\times}10^4$. The flow is therefore turbulent and at the velocity measurement plane the boundary layers are fully developed (or at least nearly so) in the absence of MHD interaction.

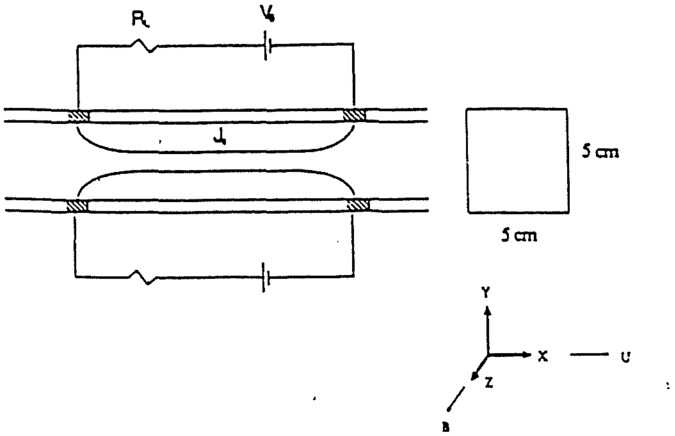

Figure 4 *Electrical Configuration for Hall-type Channel.*

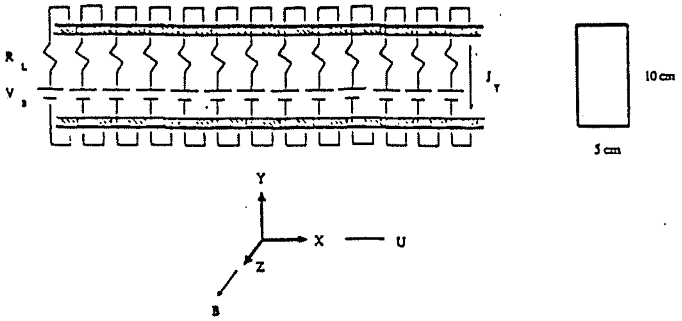

Figure 5 *Electrical Configuration for Segmented Faraday Channel.*

3.2 Electrical Configurations

For the Hall-type configuration, a pair of electrodes at the upstream end was connected through an external load to a pair of electrodes at the downstream end. Figure 4 shows the electrical configuration used to drive the axial current. The primary power source was banks of batteries (120 V per bank) providing a total of 120 - 600 V, connected in series with variable load resistors that were used to fine tune the current level. For this configuration, an appropriate definition of the magnetic interaction parameter, S_H, is

$$S_H = \frac{I_x BL}{\dot{m} U_b} ,$$

where I_x is the applied axial current, L is the distance from the upstream electrode to the measurement plane, $\dot{m}$ is the mass flow rate, and U_b is the mean axial velocity. The interaction parameter in this form represents the ratio of the transverse Lorentz force to the axial inertia of the flow. We thus expected the secondary flow to be sensitive function of this parameter.

Figure 5 shows the segmented Faraday configuration used in the most recent series of experiments. The active channel had thirteen electrode pairs each with a 120-240 V battery power supply and series load resistance. For this configuration, the magnetic interaction parameter is defined as

$$S_P = \frac{J_y B L}{\rho U_b^2} \quad .$$

The interaction parameter S_P is therefore a measure of the ratio of the axial Lorentz force to the axial inertia of the flow. Although S_P is not directly related to the transverse Lorentz force that drives the secondary flow, it is a parameter that indicates the relative strength of the electromagnetic body forces acting on the fluid flow.

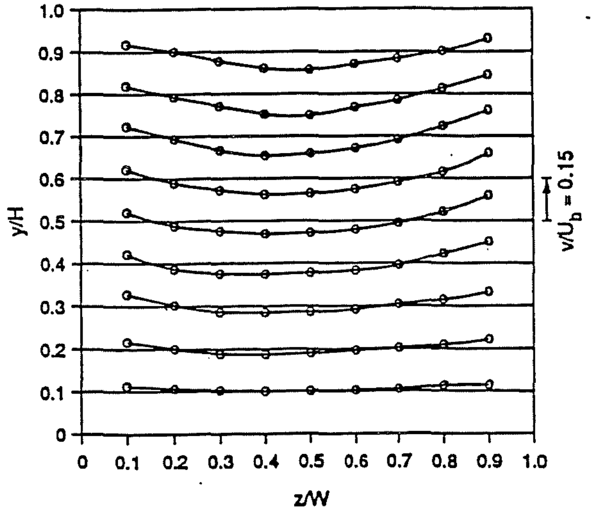

Figure 6 *y-Directed Velocity for S_H=0.5.*

4. SUMMARY OF HALL EXPERIMENTS

In this section we review the major results of the experiments run in the Hall-type configuration. In addition, we use a simple two-dimensional model to help explain the features of the experimental results.

4.1 Experimental Results

The y-directed component of the velocity, V_y, has been measured for interaction parameters ranging from S_H=0 to S_H=2.4. Figure 6 shows the cross-plane distribution of V_y for S_H=0.5. In this figure, points above the horizontal grid lines represent positive velocities and points below the lines represent negative velocities where one full unit equals 15% of the average axial velocity. The two-cell rotation of the fluid in the cross-plane expected from a first order model of the secondary flow mechanism is evident in these data. The secondary flow is, however, much stronger in the upper region of the channel than the bottom. This was a surprising result since the secondary flow pushes the hotter, more conductive, fluid down in the channel and thus the transverse Lorentz force is larger in the bottom region.

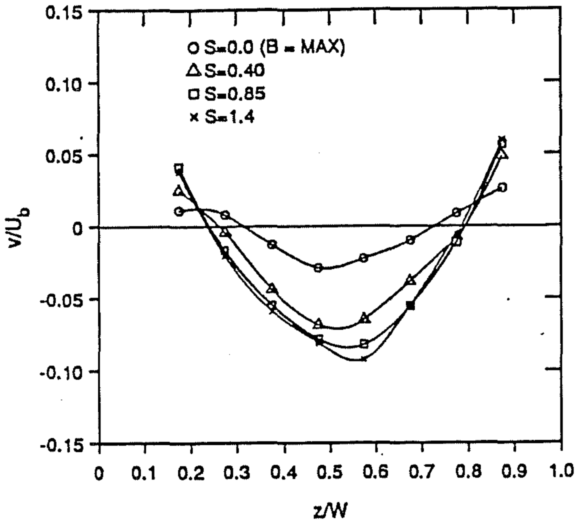

Figure 7 *Transverse Velocity Profiles (y/H=0.7).*

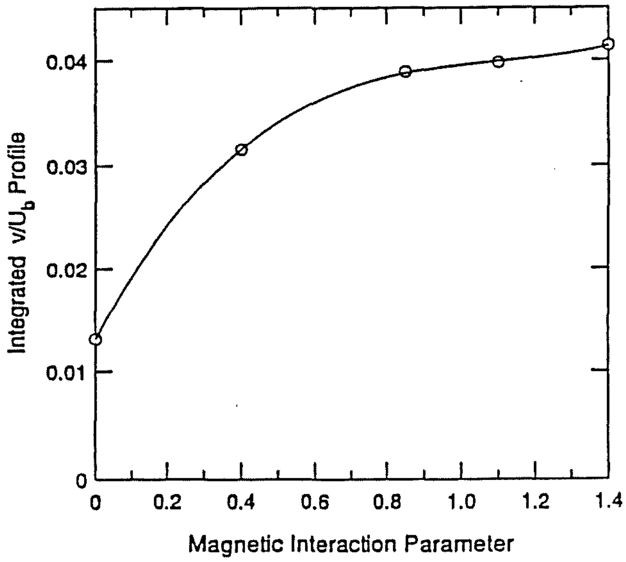

Figure 8 *"Saturation" of Secondary Flow.*

Results at other interaction levels for which we have made measurements show no qualitative changes in the structure -- only the magnitude of the secondary flow changes. Figure 7 shows z-profiles of V_y for several interaction levels at a normalized height in the channel of 0.7. In this figure the S_H=0 profile is for no applied current but full magnetic field and the transverse velocities are the result of Lorentz body forces arising from Hartmann currents. As a measure of the magnitude of the secondary flow, Figure 8 shows the area bounded by each velocity profile and the V_y = 0 line, plotted versus interaction parameter. The magnitude of the secondary flow is initially a sensitive function of interaction parameter but above S_H=0.85 reaches a "saturation" condition where further increases in interaction level show little or no corresponding increase in the level of secondary flow.

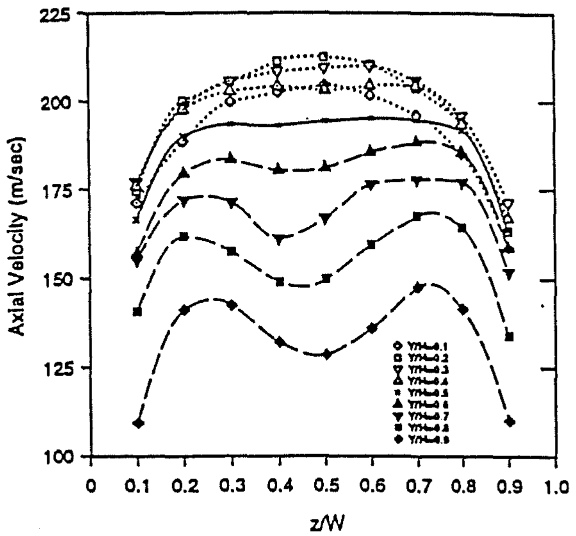

Figure 9 *Axial Velocity Profiles for S_H=0.5.*

The axial component of the velocity, V_x, has also been measured for the range of interaction levels S_H=0 to 2.4. Figure 9 shows the results for S_H=0.5. These axial velocity z-profiles show pronounced "M"-shapes in the upper portion of the channel. The "M"-shapes occur because secondary flow vortices convect the slower moving sidewall fluid into the center. In the bottom region, the profiles flatten as the warmer fluid that was in the y-center of the channel is swept to the sidewalls. Note also that the secondary flow shifts the peak velocity down in the channel. For S_H=0.5, the axial velocity peak occurs at a normalized height in the channel of approximately 0.2.

4.2 Two Dimensional Model

We have developed a simple two dimensional model that helps explain the concentration of vorticity in the upper region of the channel and provides insight into the mechanism for "saturation" of the secondary flowfield. The model assumes a fully developed MHD flow between semi-infinite parallel plates as shown in Figure 10. If we neglect axial gradients and note that for the semi-infinite geometry assumed, the z-component of the velocity and all y-derivatives are zero, the y-momentum equation is

$$0=-\frac{\partial P}{\partial y}+\frac{\partial}{\partial z}\left[\mu\left(\frac{\partial v}{\partial z}\right)\right]-J_x B \quad ,$$

which, assuming constant viscosity, we may twice integrate. The solution is then

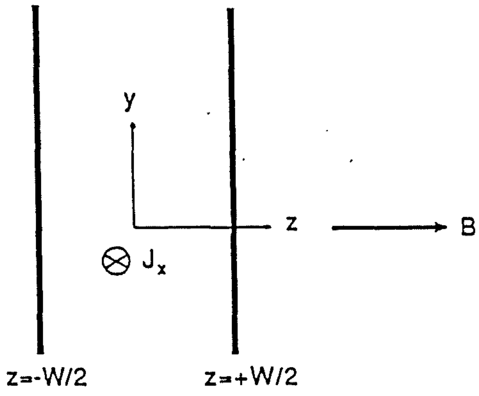

Figure 10 *Two-Dimensional Model Schematic.*

$$v=\frac{1}{\mu}\int_0^{z}\int_0^{z''}\frac{\partial P}{\partial y}dz'dz''+\frac{B}{\mu}\int_0^{z}\int_0^{z''}J_x dz'dz''+v_d \quad , \qquad (1)$$

where v_d is the y-directed velocity at the z-center of the channel.

The solution shows that the secondary flow is due to a balance between the y pressure gradient and the transverse Lorentz force. To use this model to explain phenomena observed in the M-2 channel, the axial current distribution is calculated from the measured velocities at a given height in the channel using the Reynolds analogy and the procedure described in reference 6. An assumption must be made about the shape of the y pressure gradient. We assume a parabolic nonuniformity in ∂P/∂y:

$$\frac{\partial P}{\partial y}=A_1+A_2 z^2 \quad .$$

Three equations are then required to evaluate the three unknown constants A_1, A_2, and v_d. The first is the boundary condition at the walls:

$$v\left(\pm\frac{w}{2}\right)=0 \quad ,$$

which gives

$$v_d=-\frac{1}{\mu}\frac{\partial P}{\partial y}\frac{w^2}{8}-\frac{B}{\mu}\int_0^{\frac{w}{2}}\int_0^{z''}J_x dz'dz'' \quad .$$

The second condition is a continuity condition. In the actual channel there are top and bottom walls and therefore the net mass flow across any constant-y line must be zero, assuming negligible axial gradients. This condition is written as

$$\int_0^{w/2} v\,dz=0 \quad ,$$

or from equation (1)

$$\frac{1}{\mu}\frac{\partial P}{\partial y}\frac{w^3}{48}+\frac{B}{\mu}\int_0^{w/2}\int_0^{z'''}\int_0^{z''} J_x dz' dz'' dz''' + v_d\frac{w}{2}=0 \quad .$$

The final relation is obtained by evaluating the y-momentum equation at the z-centerline neglecting axial gradients and noting that by symmetry $\partial v/\partial z = 0$ and that $\partial^2 v/\partial z^2$ is small compared to the axial current and pressure terms. The result is

$$v(0)\frac{\partial v}{\partial y}(0)=-\frac{1}{\rho}A_1+\frac{\mu}{\rho}\frac{\partial^2 v}{\partial z^2}(0)-\frac{J_x(0)B}{\rho} \quad .$$

The convective acceleration term and the stress term are also generally small at the z-centerline, except very near the top and bottom walls, but they are retained since they are simple to evaluate using polynomial curve fits of the measured vertical velocity data. Note that at the z-centerline, the y pressure gradient must very nearly balance the local value of the transverse Lorentz force.

We must also make an estimate of the turbulent viscosity. For a fully developed turbulent channel flow, it is customary to divide the flow into three layers: an inner layer where viscous shear is dominant, an overlap layer where both viscous and turbulent shear are significant, and an outer layer where turbulent shear is dominant. The outer layer typically occupies over 80% of the channel width. In this region the effective viscosity is nearly constant and much larger than the molecular viscosity. Clauser[8] proposed that the turbulent viscosity in the outer layer could be scaled by the displacement thickness δ^* and the freestream velocity U_∞:

$$\mu_t \approx K\,\rho\,U_\infty\,\delta^* \qquad (2)$$

where K is a dimensionless constant taken to have an average value 0.016[9]. For our channel flow, the displacement thickness calculated from the measured axial velocity distribution for a non-MHD case is approximately 0.6 cm. Equation (2) then gives a turbulent viscosity $\mu_t \approx 0.0025$ Pa-sec which we use for the whole channel width.

Figure 11 shows the calculated vertical velocity flowfield for an interaction parameter of S_H=0.5 . The model correctly predicts the concentration of the vorticity in the upper region of the channel despite the concentration of the transverse Lorentz force in the bottom region. Figure 12 shows the corresponding pressure gradient distribution. The nonuniformity in the pressure acts to enhance the vorticity in the upper region of the channel and reduce it in the bottom.

A comparison of the calculations to the experimental measurements (Figure 6) shows rather remarkable qualitative agreement considering the simplicity of the model and the complexity of the actual flowfield. For higher interaction parameters, however, the nonuniformity in the y pressure gradient calculated by the model is not sufficient to suppress the secondary flow in the bottom region although it apparently is in the actual flow. This result is probably due to the assumed parabolic shape of the pressure distribution, which may not be reasonable at higher interaction levels.

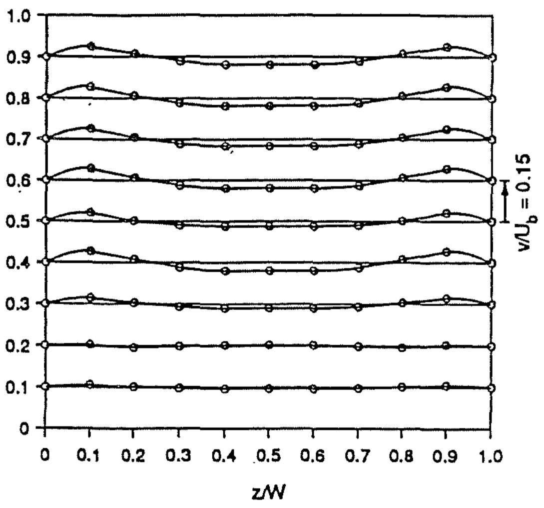

Figure 11 *Two-Dimensional Model Calculated V_y.*

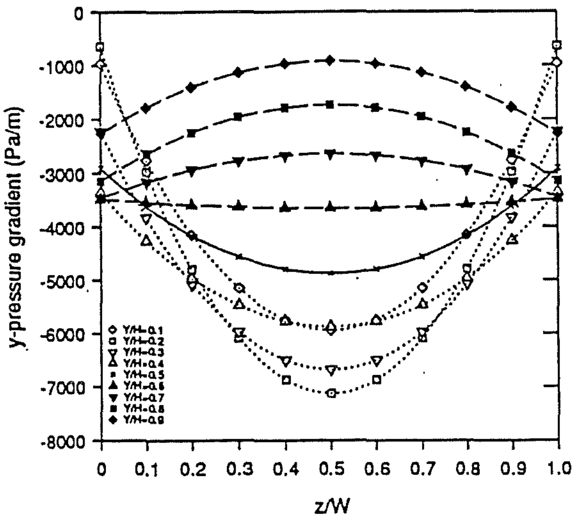

Figure 12 *Two-Dimensional Model Calculated $\partial P/\partial y$.*

A quantitative comparison shows that the model underpredicts the magnitude of the secondary flow. Since the solution scales linearly with the reciprocal of the turbulent viscosity, it is possible that the estimated μ_t is too large. The value used was calculated using an empirical formula (equation (2)) developed for non-MHD flows. In MHD flows the effective viscosity may be different due to turbulence suppression[10] and other effects.

The model successfully explains the concentration of the vorticity in the upper region of the channel in terms of the nonuniform pressure gradient that must in an overall sense

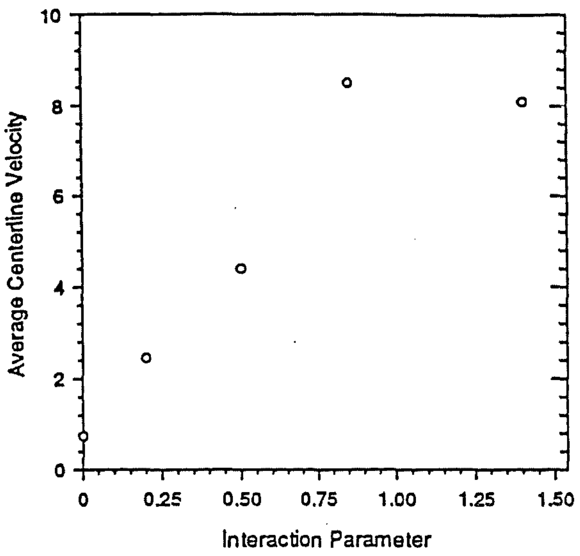

Figure 13 *Two Dimensional Model Secondary Flow Sensitivity to S_H.*

balance the transverse Lorentz force. The observed "saturation" of the secondary flow is a little more complicated. It is clear that flowfield coupling strongly distorts the axial current distribution and thus alters the driving force for the secondary flow. If the balancing pressure field was not also distorted by coupling with the secondary flow, a condition could be reached where the net driving force in the top region could drive a reverse vortex compared to the original sense. For the actual flow, however, in the top region of the channel the nonuniformity in the y-pressure gradient counteracts the increasing distortion of the transverse Lorentz force and a sort of balance appears to be reached. The distorted transverse Lorentz force profile that would tend to drive a reverse vortex is compensated by the distortion of the y-pressure gradient profile. In the bottom region of the channel, the nonuniformity in the y-pressure gradient balances the nonuniformity in the transverse Lorentz force throughout the whole range of interaction parameters for which data has been obtained. Figure 13 shows the calculated average centerline velocity in the top half of the channel plotted versus interaction parameter. The model does appear to show the "saturation" of the secondary flow although some intermediate points would be helpful.

5. RESULTS OF SEGMENTED FARADAY EXPERIMENTS

In this section we present the results of the most recent series of experiments. For these experiments the channel was configured as a segmented Faraday generator with 13 electrode pairs and a 5 x 10 cm^2 cross-section.

Figures 14, 15, and 16 show the measured secondary flows for interaction parameters S_P = 0 (Hartmann case), 0.4, and 0.55. The secondary flows are similar in magnitude to those measured for the Hall configuration but they are not as sensitive a function of interaction parameter. The structure of the secondary flowfield is also similar to that for the Hall configuration rather than the 6-cell pattern predicted from the first-order mechanism described earlier. We do, however, apparently see a 4-cell pattern for S_P=0.55, with a pair of vortices near the cathode (y/H=0.1) rotating in the opposite sense to the two main vortices.

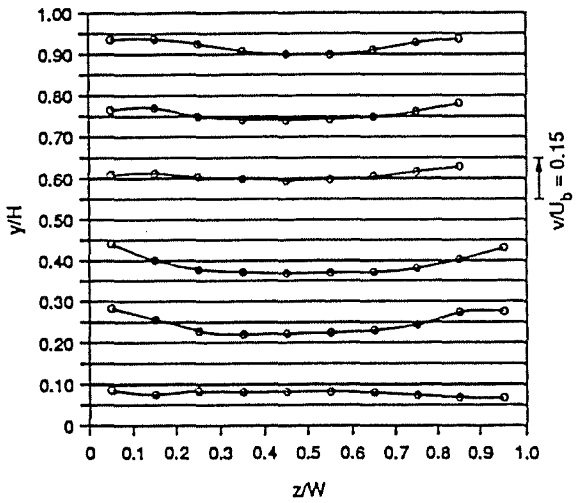

Figure 14 *y-Directed Velocity Distribution for S_F=0.*

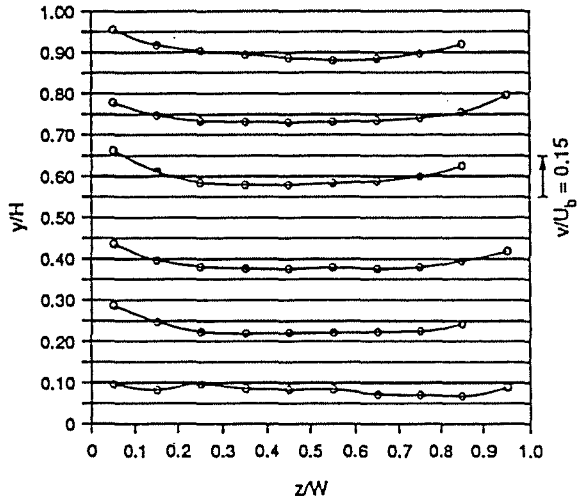

Figure 15 *y-Directed Velocity Distribution for S_F=0.4.*

Figures 17, 18, and 19 show the measured axial velocity profiles for a non-MHD case and for S_F=0.55. For the S_F=0.55 case, an "M"-shaped axial velocity profile appears near the anode (top) wall as the secondary flow vortices convect the slower sidewall fluid into the center. In the bottom half of the channel we again see an "M"-shaped profile but it is displaced from the cathode wall.

In addition to distorting the axial velocity profiles, the

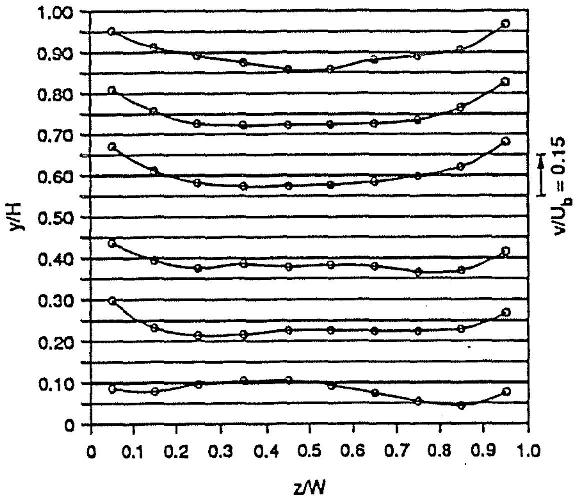

Figure 16 *y-Directed Velocity Distribution for S_F=0.55.*

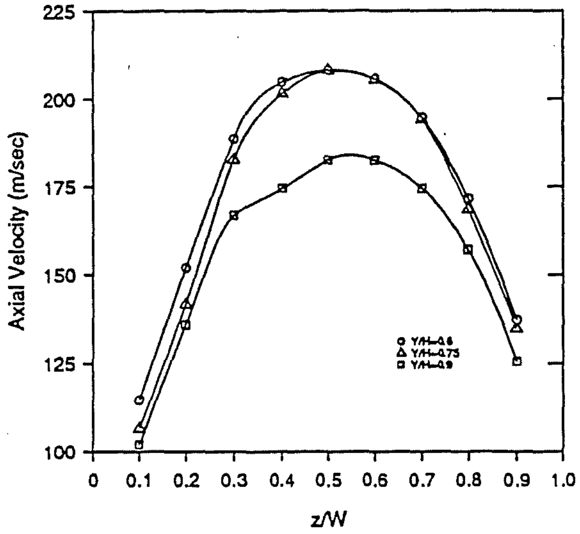

Figure 17 *Axial Velocity Distribution in Top Half of Segmented Faraday Channel for non-MHD case.*

secondary flow affects the electrode temperatures and boundary layer voltage drops. Figures 20, 21, and 22 show the change in electrode temperatures relative to a baseline non-MHD case, for interaction parameters S_F = 0, 0.2, and 0.4. Although there is considerable scatter in these data, we may still see that the secondary flow cools the anode and heats the cathode. This effect increases as we increase the interaction level.

The cooling of the anode and heating of the cathode have corresponding effects on the electrode boundary layer voltage drops. Figure 23 shows these voltage drops for interaction parameters S_F = 0.2, 0.4, and 0.55.

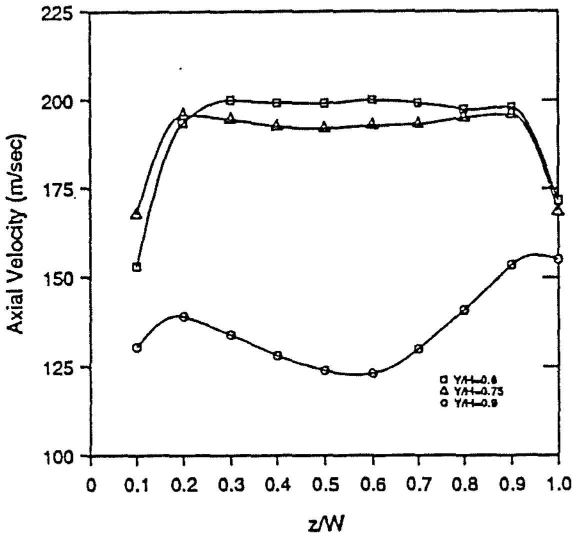

Figure 18 *Axial Velocity Distribution in Top Half of Segmented Faraday Channel with S_F=0.4.*

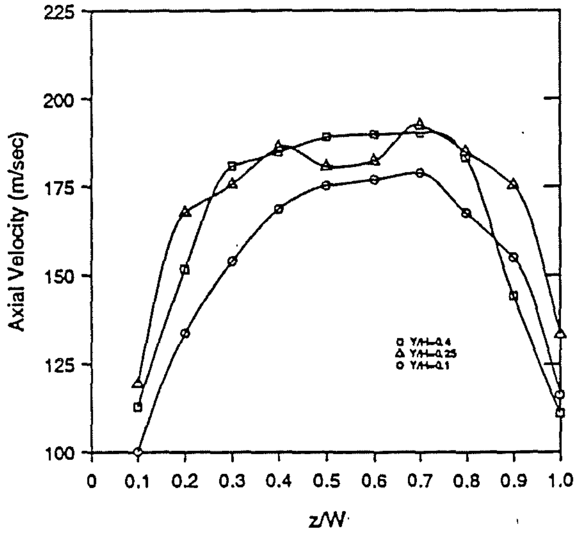

Figure 19 *Axial Velocity Distribution in Bottom Half of Segmented Faraday Channel with S_F=0.4.*

6. SUMMARY AND CONCLUSIONS

Secondary flows have been measured at Stanford for both Hall-type and segmented Faraday channels for a wide range of electromagnetic interaction levels. For the Hall-type channel experiments, the secondary flow was initially a sensitive function of electromagnetic interaction level but eventually reached a "saturation" condition where increasing the interaction level showed little or no corresponding increase in the level of secondary flow. The secondary flow was also observed to be concentrated in the upper two thirds of the channel despite a

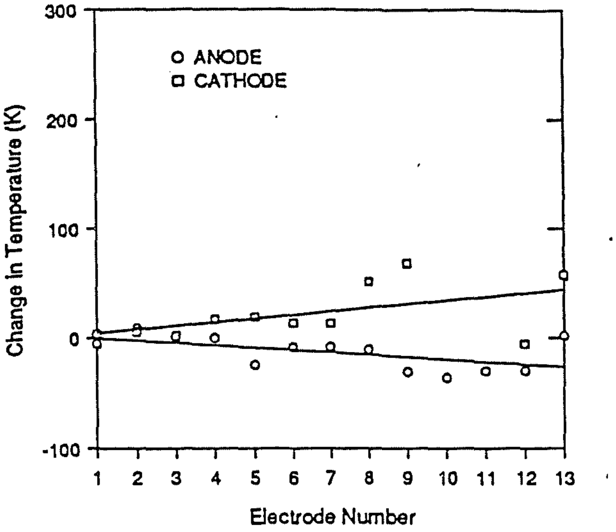

Figure 20 *Segmented Faraday Channel Change in Electrode Temperature from Baseline non-MHD case for* $S_F=0$.

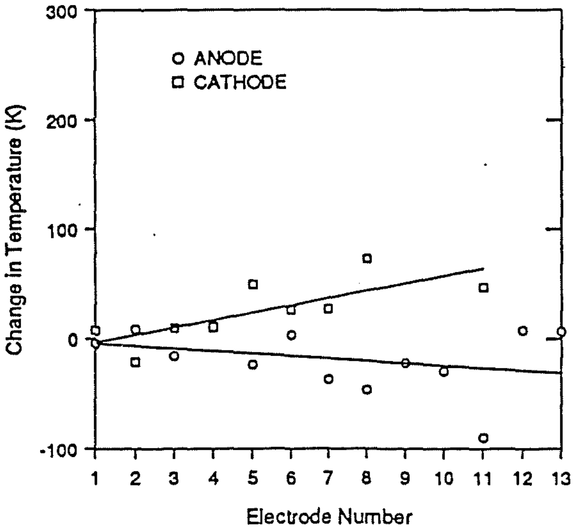

Figure 21 *Segmented Faraday Channel Change in Electrode Temperature from Baseline non-MHD case for* $S_F=0.2$.

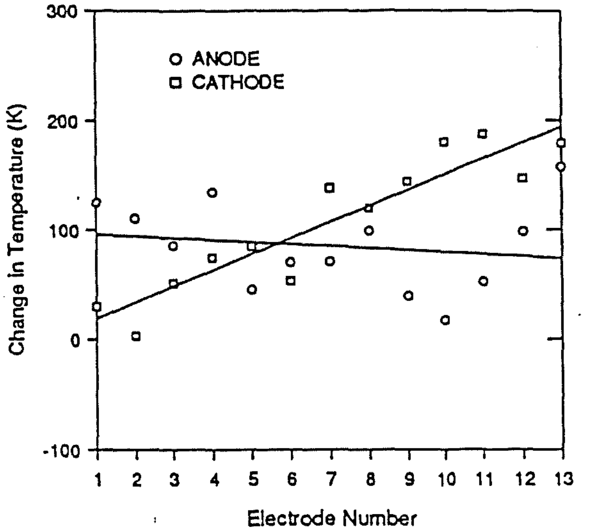

Figure 22 *Segmented Faraday Channel Change in Electrode Temperature from Baseline non-MHD case for* $S_F=0.4$.

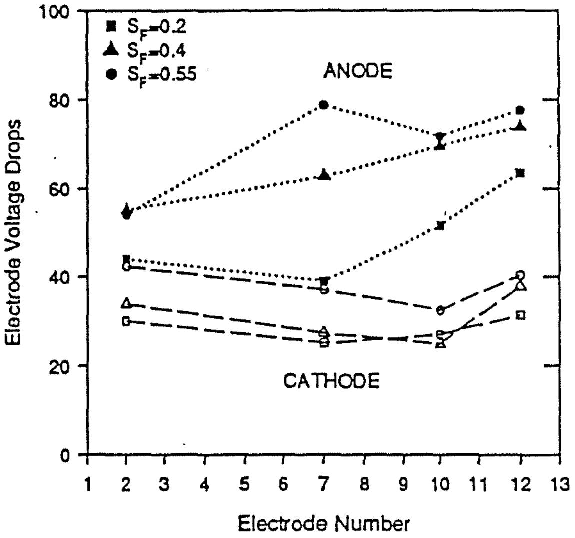

Figure 23 *Segmented Faraday Channel Electrode Voltage Drops.*

concentration of the transverse Lorentz force in the bottom region of the channel. With the aid of a simple two-dimensional model we have explained these results in terms of the coupling between the secondary flow and the transverse Lorentz force that drives it and an increasingly nonuniform y-pressure gradient.

The results of the segmented Faraday generator experiments show a 2-cell secondary flowfield for lower interaction levels which appears to develop into a 4-cell flowfield at higher interaction levels. The structure of the secondary flow depends on various competing effects. The most important effects in the Stanford channel are the y-nonuniformity in the electrical conductivity and finite segmentation effects (another possibly important factor would be axial leakage currents but voltage measurements indicate there was negligible leakage for these experiments). Work remains to be done to determine the relative importance of each of these effects in our experiments.

REFERENCES

1. Maxwell, C. D., Doss, E. D., Oliver, D. A., and Curry, B. P., "Consideration of Three Dimensional Effects in MHD Power Generators," 15th Symposium on Engineering Aspects of Magnetohydrodynamics, Philadelphia, PA, June 1976.

2. Bityurin, V. A., Zatelepin, V. N. and Lyubimov, G. A., "Effect of Force Field Nonuniformity on Flow in and MHD Channel," *Fluid Dyn.* 13, 1, 1978.

3. Doss, E. D., and Ahluwalia, R. K., "Three-dimensional Flow Development in MHD Generators at Part Load," *J. Energy* 7, 289, 1983.

4. Girshick, S. L. and Kruger, C. H., "Experimental Study of Secondary Flow in a Magnetohydrodynamic Channel," *J. Fluid Mechanics* 170, 233, 1986.

5. Goforth, R. C. and Kruger, C. H., "Measurements of the Effect of Interaction Parameter and Wall Temperature on Secondary Flow in an MHD Channel," 26th Symposium on Engineering Aspects of Magnetohydrodynamics, Nashville, TN, June 1988.

6. Goforth, R. C., Kruger, C. H., and Aoki, T., "An Investigation of Secondary Flow in an MHD Channel," 27th Symposium on Engineering Aspects of Magnetohydrodynamics, Reno, NV, June 1989.

7. Swean, T. F., Oliver, D. A., Maxwell, C. D., and Demetriades, S. T., "Prediction of Transverse Asymmetries in MHD Ducts with Zero Net Hall Current," *AIAA J.*, 19, 651, 1981.

8. Clauser, F. H., "The Turbulent Boundary Layer," *Adv. Appl. Mech.* 4, 1, 1956.

9. White, F. M., *Viscous Fluid Flow*, McGraw-Hill, 1974.

10. Reis, J. C. and Kruger, C. H., "Turbulence Suppression in Combustion-Driven Magnetohydrodynamic Channels," *J. Fluid Mechanics* 188, 147, 1988.